Accepted for publication in *The Astrophysical Journal*

On the Non-relativistic Origin of Red-skewed Iron Lines in CV, Neutron Star and Black Hole Sources

Lev Titarchuk[1], Philippe Laurent[2] & Nikolai Shaposhnikov[3,4]

ABSTRACT

We perform the analysis of the iron K_α lines detected in three sources representing of three types of accreting compact sources: cataclysmic variable (CV) GK Per, neutron star (NS) Serpens X-1 and black hole (BH) GX 339-4. We find, using data from Epic-PN Camera on-board XMM-*Newton* observatory, that the iron K_α emission line in GK Per has a noticeable red-skewed profile. We compare the GK Per asymmetric line with the red-skewed lines observed by XMM-*Newton* in Serpens X-1 and GX 339-4. The observation of the K_α emission with red-skewed features in CV GK Per cannot be related to the redshift effects of General Relativity (GR). Therefore, if the mechanism of the $K_\alpha-$line formation is the same in CVs, NSs and BHs then it is evident that the GR effects would be ruled out as a cause of red skewness of K_α line. The line reprocessing in an outflowing wind has been recently suggested an alternative model for a broad red-shifted iron line formation. In the framework of the outflow scenario the red-skewed iron line is formed in the strong extended wind due to its illumination by the radiation emanating from the innermost part of the accreting material. The outflow is a common phenomenon for CVs, NSs and BHs. In this Paper we demonstrate that the asymmetric shapes of the lines detected from these CV, NS and BH sources are well described with the wind (outflow) model. Furthermore we find by analyzing *RXTE* observations that when the strong red-skewed iron

[1]George Mason University, Fairfax, VA 22030; US Naval Research Laboratory, Code 7655, Washington, DC 20375-5352; Goddard Space Flight Center, NASA, code 663, Greenbelt MD 20771, USA and Physics Department, University of Ferrara, Via Saragat, 1 44100 Ferrara, Italy; lev.titarchuk@nrl.navy.mil

[2]CEA/DSM/DAPNIA/SAp, CEA Saclay, 91191 Gif sur Yvette, France;plaurent@cea.fr; Laboratoire APC, 10 rue Alice Domont et Leonie Duquet, 75205 Paris Cedex 13, France

[3]University of Maryland, Astronomy Department, College Park, MD 20742

[4]CRESST/GSFC/NASA, code 662, Greenbelt MD 20771

line is observed in GX 339-4 the high frequency variability is strongly suppressed. While this fact is hard to reconcile with the relativistic models, it is consistent with the outflowing gas washing out high frequency modulations of the radiation presumably originated in the innermost part of the source.

Subject headings: line: profiles —stars: white dwarfs, neutron —X-ray :binaries — X-rays: individual (GK Per), individual (Serpens X-1), individual (GX 339-4) —radiation mechanisms—physical data and processes

1. Introduction

The K_α iron line is emerging as one of the most important probes of physical processes near accreting compact objects, which include black holes (BH), neutron stars (NS) and white dwarfs (WD). Strong red-skewed iron lines have been reported in multiple observations of BHs (Miller 2007) and CVs (Hellier & Mukai 2004), hereafter HM04. With a discovery of a red-skewed iron line in the NS source Serpens X-1 by Bhattacharyya & Strohmayer (2007), hereafter BhS07, the asymmetric lines have now been observed in all types of accreting compact objects. In this Paper we analyze the line profiles in CV (WD) GK Per, NS Serpens X-1 and BH GX 339-4 as representatives of each compact object sub-class. The reason for such a study is simple: if the Physics leading to the asymmetry of the iron line profile in all types of compact objects is the same, it will allow us to put additional constrains on the iron line formation models.

HM04 presented the compilation of Fe $K_\alpha-$line spectra of 5 magnetic CVs using the Chandra High-Energy Transmission Grating (HETG). The GK Per fluorescent line had the highest signal-to-noise ratio. HM04 demonstrated that the K_α iron line in GK Per showed a Doppler-shifted red wing extending to 6.33 keV which they attribute to pre-shock material falling with at near WD escape velocity. They also detected a fainter, 170-eV shoulder which, they suggested, may be due to Compton downscattering.

BhS07 reported on an analysis of XMM-Newton data from NS low-mass X-ray binary (LMXB) Serpens X-1 (Ser X-1). Their spectral analysis of EPIC PN data indicates that the previously known broad iron K_α emission line from this source has a skewed structure with a moderately extended red wing. The BhS07 finding suggests that the broad lines seen in other NS LMXBs would likely have the skewed shape as well, the origin of which is still under debate. In fact, BhS07 showed that the quality of fits of observed red-skewed lines in NSs are the same for both the "diskline" model [see Fabian et al. (1989)] related to Schwarzschild potential and for the "Laor" model [see Laor (1991)] related to a maximally spinning BH.

It implies that the red-skewed line is not a particular signature of a maximally spinning black hole given that this shape is also common to the lines from NS sources. Subsequent *Suzaku* observation of three NS LMXBs (Ser X-1, 4U 1820-30 and GX 349+2) analyzed by Cackett et al. (2008) have shown broad, asymmetric, iron emission lines in all three objects. These iron K_α lines can be also well-fitted by the model for lines from a relativistic accretion disk (diskline), and by the 'Laor' model. Miller (2007) reviewed observations of red-shifted line from BH sources and their interpretation in terms of the relativistic models.

The iron fluorescence related to the reflection of hard (power law) spectrum from the cold accretion disk have been the most widely studied model for asymmetric emission line formation [see Reynolds & Nowak (2003) and Miller (2007)]. However, all theoretical alternatives have to be explored and properly dismissed before indisputably claiming of such an important physical effect as General Relativity (GR) as an origin of this redskewed line phenomenon. As we show in this Paper, the GR interpretation of the red-skewed lines in NSs and BHs is not an unique model which successfully describes the observed line profiles. An alternative viable explanation of the line properties can be achieved in terms of downscattering of line photons in the wind outflows which are commonly produced in these systems.

A model for red-skewed emission lines by repeated electron scattering in a diverging outflow or wind was considered by Titarchuk et al. (2003), Laming & Titarchuk (2004), and Laurent & Titarchuk (2007), hereafter LT04, LT07 respectively. Let us remind the reader the geometry of the wind model. It is assumed the wide-open wind is launched at some disk radius R_W where presumably the local radiation force $\sigma L(R_W)/c$ exceeds the local disk gravity $m_p HGM/R_W^3$ [see e.g. Titarchuk et al. (2007)]. Here $L(R_W)$ is the disk local luminosity at R_W, σ is an effective plasma cross-section which is, in principle, greater than the Thomson electron cross-section $\sigma_{\rm T}$; H is the half-height of the disk, and m_p is the proton mass. Thus this wind should be illuminated by the emission of X-rays formed in the innermost part of the source. The $K_\alpha-$line is generated in a narrow wind shell and the line profile is formed in the partly ionized wind when $K_\alpha-$line photons are scattered off the diverging flow (wind) electrons. Electron scattering of the Fe K_α photons within the highly ionized expanding flow leads to a decrease in photon energy (redshift), which is of the first order in $\beta_W = V_W/c$, when V_W is the outflow velocity with $V_W \ll c$. This photon redshift is an intrinsic property of any outflow for which divergence is positive.

LT07 fitted the Monte-Carlo (MC) model line profiles to the observations using just three free parameters: β_W, the optical depth of the wind τ_W and the wind plasma temperature T_W. LT07 showed examples of the outflow model fitted to the XMM observation of MCG 6-30-15 (Wilms et al. 2001) and to the ASCA observations of GRO J1655-40 (Miller et al.

2004a). The red-skewed part of the spectrum is formed by photons undergoing multiple scatterings while the primary peak is formed by photons escaping directly to the observer.

There are two completely independent lines of reasoning motivating a consistent study of the asymmetric Fe lines in WDs, NSs and BHs. The first comes from the fact that certain theoretical alternatives to relativistic disk interpretations in the BH and NS sources, namely those alternatives based on wind outflow geometries, are not restricted to those classes of accreting compact objects but could readily include accreting cataclysmic variables (CV), meaning an appropriate subset of WDs. However, there is a second point which is more general. Just as the NS case cannot be modeled appropriately with a near-maximal Kerr metric because the NS precludes such a high angular momentum, a WD case would have to be modeled with a disk whose gravitational potential was effectively Newtonian, far from relativistic regions of the Schwarzschild metric. Thus, within the context of the more popular disk models and without any reference to any alternative models such as outflow, it would force a re-examination of some of the basic assumptions.

We analyze the K_α lines observed in the GK Per, Ser X-1 and GX 339-4 with XMM-*Newton*. For GX 339-4 we also analyze simultaneous *RXTE* data. We model the line profiles both in terms of relativistic models and in terms of wind/outflow paradigm. Additionally, we consider GX 339-4 XMM-*Newton*/*RXTE* observations in terms of broader context of line behavior with respect to fast source variability which provides additional information on the system geometry and allows to constrain line formation models.

We present observations and the data analysis in §2. In §3 we discuss our results and their implications to theoretical models. Conclusions follow in §4.

2. Observations and Data Analysis

The primary instrument for our study of the iron line profiles is the XMM-*Newton*/Epic-PN camera. We also use *RXTE* observations as supporting spectra and timing data. The corresponding data sets were downloaded from HEASARC[1] and analyzed following the "SAS User's Guide" using `especget` SAS tool. For GK Per we use XMM observation on March 9 2002 (ID 0154550101/revolution 412). The Epic cameras were operating in the full imaging mode during this observation. We extracted the source spectrum from a circular region centered on the GK Per position with a radius of 35 arcsec and we extracted a background spectrum from a nearby source free region. In addition, we present the *RXTE* spectrum

[1]http://heasarc.gsfc.nasa.gov/

of GK Per from the observation on March 8, 2002 (Obs ID 70401-01-02-00) which was the closest to that by XMM.

We use the XMM-*Newton* observations of NS Ser X-1 (XMM rev. 785), and BH GX 339-4 (see §2.3 for details of the XMM/*RXTE* observations). XMM/Epic-PN data for Ser X-1 and GX 339-4 were collected in the timing mode, for which spacial information is available for one dimension (RAWX) only. We extracted source and background spectra from stripes according to selection criteria 10<RAWX<60 and 2<RAWX<9 correspondingly. For the GX 339-4 observations we also used simultaneous *RXTE* data. We extracted PCA and HEXTE energy spectrum from standard *RXTE* data modes. For spectral analysis we use the energy ranges 1.0-10.0, 9.0-30.0 and 20.0-200.0 keV for *XMM*/Epic-PN, *RXTE*/PCA and *RXTE*/HEXTE spectra correspondingly. *RXTE* response matrices were calculated using XTE FTOOLS package and "RXTE Cook Book" recipes. For timing analysis we calculated Fourier power density spectrum (PDS) from the high timing resolution *RXTE* data modes in the frequency range 0.05 to 256 Hz.

Spectral analysis was performed using XSPEC astrophysical spectral modeling package. The models applied to the data and the results of spectral fits are shown in Tables 1-4. Spectral shapes for observations of GK Per, Ser X-1 and GX 339-4 (Observations 1 and 2) indicate the presence of a strong iron emission line. We apply three models for the iron line: DISKLINE, LAOR and WINDLINE. Note DISKLINE and LAOR are standard XSPEC models. The DISKLINE model describes the line emission produced by a relativistic accretion disk (Fabian et al. 1989). The LAOR component presents the line from an accretion disk around a black hole including GR effect calculated by Laor (1991). The WINDLINE model is a Monte-Carlo code simulating the downscattering of the iron line photons in a diverging wind from a compact object as per Laurent & Titarchuk (2007). The code was ported into XSPEC as a local model.

2.1. GK Per

Cataclysmic variables (CVs) are interacting binaries in which the accreting object (the primary) is a white dwarf [see Warner (1995) for a review]. X-ray emission in CVs is most likely associated with the accretion process, which is capable to heat accreted material at a shock up to high temperatures (kT ∼5-20 keV). Thus one can fit the continuum spectrum of GK Per emission by the model in which the soft photons originated in the accretion disk (or at the WD surface) are upscattered (Comptonized) off hot electrons of the plasma cloud (shock region).

Given that, we use the Comptonization model by Titarchuk (1994) and Hua & Titarchuk (1995) (see COMPTT model in XSPEC) to infer the electron temperature T_e and the optical depth τ_e of the plasma cloud where the emergent spectrum of GK Per is produced. Unfortunately, there is no simultaneous observations of GK Per by XMM and *RXTE* therefore we choose the nearest *RXTE* observations to estimate the model for continuum emission which we then can use as a starting model to fit the XMM data. In Figure 1 we present the *RXTE*/PCA spectrum of GK Per fitted by the model WABS∗(COMPTT +GAUSSIAN). The best parameters of the model are hydrogen column $n_H \sim 1.5 \times 10^{22}$ cm^{-2} (frozen), color temperature of the seed photon of COMPTT $T_0 = 0.5$ keV (frozen), plasma temperature of the Compton cloud (CC) $kT_e = 5.1 \pm 0.2$ keV, CC optical depth $\tau_e = 25 \pm 5$, the energy of the Gaussian line $E_L = 6.1 \pm 0.3$ keV, the line width $\sigma = 0.8 \pm 0.1$ keV. The model is acceptable given that $\chi^2 = 73.6/77 = 1.04$. The above COMPTT best-fit parameters correspond to the spherical geometry of Compton cloud.

HM04 reported the results of their analysis of *Chandra* HETG data from GK Per. Specifically they pointed out that Fe K$_\alpha$ fluorescent line exhibits an extended red wing. The Chandra spectrum of GK Per (see Fig. 1 in HM04) may also indicate the presence of 6.7 keV and weak 6.96 keV lines, that is presumably the Fe$_{XXV}$ (He-like) and Fe$_{XXVI}$ (H-like) lines respectively. In our analysis we confirm that the Fe K$_\alpha$ line in GK Per is asymmetric. However, XMM data do not show any evidence for the 6.7 and 6.96 keV narrow lines (see Table 1).

We first tried to fit the XMM-*Newton* spectrum from GK Per with the model WABS∗-(BBODY + COMPTT)∗EDGE. We find that the quality of the fit using this model is unacceptable, $\chi^2/dof = 2.4$ and also we find a strong red-skewed residual in the energy range between 5 and 7 keV. Addition of the GAUSSIAN with the energy ~ 6.4 keV leads to the improvement in the fit quality to $\chi^2_{red} = 1.5$, which is still unsatisfactory. This indicates that the line profile is not symmetric. We then replaced GAUSSIAN with a physically motivated model to fit the asymmetric iron line, i.e. DISKLINE, LAOR or WINDLINE model. We were able to obtain acceptable fit quality for all models. However, the best fit statistic of $\chi^2/dof = 1.14$ is given by the WINDLINE model. The quality of the model fit to the data for the WINDLINE model is also shown in Figure 2 (lower panel) where we present the count spectrum (error bars) vs model (solid line) along with the residual in units of $\chi-$deviation of the model from the data, i.e. $\chi = (\mathrm{data} - \mathrm{model})/\sigma$. In the upper panel of Figure 2 we show the resulting photon spectrum along with its continuum and line components. The red wing of the line extended from 6.4 keV down to 5.8 keV (half width of half maximum HWHM$\sim$ 0.6 keV) is broader than the blue wing that HWHM of 0.3 keV. The same model fit with the LAOR model is shown on Figure 3. In Table 1 we present the best-fit parameters for the continuum and line components for all three model fits.

Modeling the XMM continuum spectrum of GK Per with COMPTT yields the electron temperature $kT_e = 5.3$ keV and Thomson optical depth $\tau_e = 20.1$, which are consistent with *RXTE* spectral parameters. The reported value of the optical depth is for the spherical geometry. The best-fit absorption optical depth of the multiplicative K-edge component $\tau_{max} = 0.23$. The K-edge energy range starts at 7.1 keV.

We apply DISKLINE and LAOR models to fit the line profile only formally to demonstrate that the XMM data from GK Per can be successfully fitted with these relativistic line models. The XSPEC DISKLINE and LAOR models were designed to fit to the observable red-skewed line profile which is assumed to be a result of the General Relativity (GR) effects [see e.g. Tanaka et al. (1995)]. However, the GR effects are negligible in the WD case and thus the application of the GR models to fit the red-skewed iron lines of GK Per *cannot provide physically meaningful results*. The best-fit values of the disk inner radius are $R_{in} = 12.5,\ 22R_G$ for LAOR and DISKLINE models respectively. These values are 3 orders of magnitude less than the WD radius that is about 10^9 cm. In fact, we present the fitting results for WD source using the GR models to demonstrate that *a good quality fit of the line profile by the relativistic models can not be considered as a reliable observational evidence of the GR effects*. This fact has an important consequence for the results of application of the relativistic models to NS and BH spectra. Namely, a success of these models solely based on the GR effects to fits the iron line profiles in NS and BH systems cannot serve as a solid grounds for claims that these effects are at work in these systems.

On the other hand the WINDLINE model is a physically justified model for the line production in GK Per. This model includes both scattered and direct components of the line. The free parameters of the wind model are the dimensionless wind velocity $\beta_W = V_W/c$, Thomson optical depth of the wind τ_W, plasma temperature of the wind T_W and the line energy E_L. The fit of the model [WABS∗(BB + COMPTT +WINDLINE)∗ EDGE] to the spectral data of GK Per observed by Epic-PN XMM (see Fig. 2 and Table 1) provides the best-fit values of the wind model components, specifically $\beta_W = (0.71 \pm 0.06) \times 10^{-2}$, $\tau_W = 1.46 \pm 0.06$ and $kT_W = 0.97 \pm 0.06$ keV. Apart from the unphysical outcome produced by DISKLINE and LAOR models, the best-fit parameters of the WINDLINE models represent a conceivable situation for an accreting WD system.

2.2. Ser X-1

To resolve the iron line profile in EPIC-PN data for Ser X-1 (XMM rev 785) we follow the same procedure that we apply for the analysis of the GK Per data. These data were analyzed by BhS07 who first reported the red-skewed line in a NS source. They interpreted

the asymmetric shape of the line in terms of GR line models (LAOR and DISKLINE). Consequently they suggested this broad asymmetric line in NS likely originated from the innermost part of the disk that was similar to the interpretation of the red-skewed lines observed in BH sources.

We fit three models to the data for which we use LAOR, DISKLINE and WINDLINE components to describe the iron line profile. The best-fit values of parameters and goodness of the fit for each model are shown in Table 2. The fit quality are not significantly different for all models. In Figure 4 we present the iron line profile which we find in Ser X-1 with the WINDLINE model. The upper panel shows the data (error bars) vs model (solid line) where we also show each spectral components separately. The lower panel displays the count spectrum along the residual of the data vs model in units of $\chi = (\text{data} - \text{model})/\sigma$.

According to our results the wind velocitiy and wind optical depth in Ser X-1 are similar to that of GK Per, namely $\beta_W \sim 0.015$ and $\tau_W \sim 1.6$. However, we find that the $K_\alpha-$line energy at $E_L = 6.67$ keV instead of 6.4 keV in the case of GK Per. The best-fit values of the COMPTT component of the model, presented in Table 2, the seed photon color temperature $kT_0 = 0.5$ keV, $kT_e = 2.9$ keV and $\tau_e = 13.4$ correspond to spherical geometry of Compton cloud.

The disk inner radius R_{in} is the most important parameter of the relativistic models. In our spectral modeling with the LAOR component the best fit value of R_{in} is 1.23 in units of gravitational radius ($R_g = GM/c^2$), which is the lowest limit allowed by the model. BhS07 obtained that R_{in} varied between 4.14 and 25 R_g for the LAOR model. Note that the DISKLINE model related to the Schwarzschild background is more appropriate for NS than LAOR model where the Kerr geometry is used to describe the curved space around a maximally rotating central object. For the DISKLINE model we obtained the disk inner radius $R_{in} \sim 6R_g$ which is also the lowest limit value for this parameter set by the model.

2.3. GX 339-4

The red-skewed line has been observed in the recurrent Galactic BH transient GX 339-4 on multiple occasions at different fluxes, in different states, and with both *Chandra* and XMM-*Newton* [see Miller (2007), hereafter M07, for details of these observations and for the GR interpretation of the line origin]. In particular, Miller et al. (2004b), hereafter M04b, presented the combined analysis of XMM (rev. 514) and *RXTE* observations during a bright phase of its 2002-2003 outburst. They reported an extremely skewed Fe K_α emission line in these data.

For our analysis we select three XMM-*Newton* observations made on August 24, 2002, September 29, 2002 and March 8, 2003 which were accompanied by simultaneous *RXTE*/PCA pointing observations (see Table 3 for XMM/*RXTE* data). We further refer to these data sets as Observation 1, 2 and 3 respectively. Joint XMM-*Newton*/Epic-PN and *RXTE*/PCA/HE-XTE spectrum covers the energy band from 1 to 200 keV. *RXTE*/PCA high time resolution data allow timing analysis at time scales down to milliseconds.

Our primary goal is to study the properties of the iron $K_\alpha$line. In order to assess the general behavior of the line we first fit all three observations using the model in which the line shape is described by a simple Gaussian. The centroid energy of the Gaussian was fixed at 6.4 keV while the width was allowed to change. The fit quality χ^2_{red} along with the essential parameters of the model are presented in Table 3. Unfolded energy spectra for each observation are presented in Figure 5 (left panels) accompanied by the *RXTE*/PCA power density spectra (right panels). The Observation 3 spectrum is harder than the spectrum for Observation 2: the BMC model indices $\Gamma \sim 2.17$ and 2.54 for the former and latter cases respectively. According the Homan-Belloni's BH classification [see Homan & Belloni (2005)] during the Observation 3 the source is in the hard intermediate state (HIMS) while during Observation 1 ($\Gamma \sim 2.37$) and Observation 2 the source is in the soft intermediate state (SIMS) and high soft state (HSS) respectively.

The gaussian fits to the iron line show the strongest line ($EW = 684$ keV) during Observation 2 while the line is weakest during Observation 3. Note for Observation 3 the fit by Gaussian is good giving $\chi^2_{red} = 1.02$. As for Observation 2 the quality of the fit with a gaussian ($\chi^2_{red} = 1.27$) is worse than that for Observation 3. Observation 1 presents an intermediate case between Observations 1 and 3. This qualitative analysis indicates that during Observation 2 the line profile is not symmetric and use of more sophisticated physical models is required to adequately describe the line shape. For Observation 3 the gaussian fit adequately models the spectrum. Based on the statistical significance we can conclude that during Observation 3 the line is weak and its profile is symmetric. Also given that statistical quality of the data for both Observations 2 and 3 are comparable we can suggest that the line skewness during Observation 3, is much weaker than that for Observation 2. Thus we choose Observation 2 data for application of physical models in order to investigate the origin of the line skewness which can be either due to scattering in a wind or due to relativistic red-shift effects.

Similarly to the analysis of GK Per and Ser X-1, we apply three different models (LAOR, DISKLINE and WINDLINE) to model the redskewed iron line seen in Observation 2 spectrum. Table 4 summarizes the resulting best-values of model parameters. In Figure 6 (see lower panel) we present the model fit with WINDLINE model for which $\chi^2_{red} = \chi^2/(dof)$

has the lowest value of 1.24.

We confirm the presence of the very strong red-skewed line extended from about 4 keV to 8 keV in the data for Observation 2 by M04b (see the red-skewed line profile in upper panel of Fig. 6). However, we do not confirm expectations by Miller et al. (2004c), hereafter M04c, that the wind velocity of $V_W \sim 0.3c$ is required to fit the strong red-skewed line detected in GX 339-4. In fact, our best-fit value of $\beta_W = V_W/c$ is 0.025. However our results agree with the M04c prediction of high optical depth in the wind. We find that the best-fit value of τ_W is about 4.9 (see Table 4). Modeling the spectrum of Observation 2 using the LAOR and DISKLINE components produces values for the inner disk radius of 1.23 R_g and 6.0 R_g for the LAOR and DISKLINE models respectively. As in the case of Serp X-1, these values are, in fact, the lowest allowed values for this parameter in these models.

Note these low values of R_{in} imply that the observer should directly see the innermost region of the source during this particular observation. Thus one can expect to observe high frequency variability from the innermost region on accretion flow. However, contrary to this expectation, the *RXTE*/PCA Fourier power spectra show (see right panels on Figure 5) that during Observation 2 the high frequency variability is not present at all in the power density spectrum (PDS), see details in the discussion section. As we have already pointed out the line during Observation 3 is weaker than that during Observations 1 and 2 and the line fit by Gaussian is good which implies the symmetry of the line.

M04b interpreted the spectral data of XMM rev. 514 (our Obsercvation 2) in terms of the LAOR model. They also claimed that the ionized disk reflection component should be included in the continuum model in order to fit the data. In our analysis of the same XMM-*Newton*/*RXTE* data the reflection component is not required. This difference between our continuum spectrum and that of M04b can be explained by different components used to represent the non-thermal part of the spectrum. We apply the BMC model while M04b uses the sum of thermal and power-law components. We suspect a similar bias in a treatment of the underlying continuum in the analysis of K_α line profile in the *Beppo*SAX data from the Black Hole Candidate source XTE J1650-500 by Miniuti et al. (2004) who showed the red-skewed profile of the line and interpreted as a broad and strongly relativistic iron emission line. However, recently Montanari et al. (2009) revisited this particular set of *Beppo*SAX data from XTE J1650-500 and reported much weaker K_α line emission when BMC is used for spectral continuum. We note that BMC model, as a Generic Comptonization model, is more appropriate than empirical models based on the power law approximation of the non-thermal part of the spectrum. Specifically, in application to low energy X-ray data the power-law component predicts excessive low energy emission which then results in artificial broadening of the iron line. BMC model, as well as COMPTT model for thermal Comptonization in

case of NS, properly accounts for this low energy curvature and therefore is more relevant for the analysis of BH spectra.

In Appendix A we show that the approach used for a derivation of the Generic Comptonization Green's function (and for the Generic Comptonization model as a BMC) can be also applied to explain *an empirical determined exponential and power-law distribution of wealth and income* in the United States and the United Kingdom.

3. Discussion on Possible Origin of K_α Red-skewed Line Profiles in WD, NS and BH

In this Paper we utilize XMM-*Newton*/Epic-PN data from accreting WDs, NSs and BHs to investigate in detail the structure of a red-skewed line profile of iron K_α emission from these sources. The asymmetric iron lines from NS and BH sources has been widely studied. The detections of the red-skewed lines in a number of Galactic and extragalactic BHs have led to the conclusion that this particular red skewness of the line in BH sources is related to General Relativity (GR) redshift effects in the innermost part of BH accretion disk (Miller 2007). Moreover the recent discovery of red-skewed iron line profiles in NS sources was also fashionably interpreted in terms of relativistic reflection model (Bhattacharyya & Strohmayer 2007; Miller 2007; Cackett et al. 2008).

However, we have to note that HM04 [see also McNamara et al. (2008)] had reported, using data from the Chandra HETG, the downshifted shoulder in the $K_\alpha-$line profile of GK Per. Also Vrielmann et al. (2005) have discovered a very strong red-skewed line profile at 0.6 keV in the *Chandra* ASIC-S spectrum of GK Per. They also pointed out the constancy of all observed emission lines from GK Per including the Fe fluorescence line with spin period and they further suggest that the emission site of these lines are visible at all times and from all viewing angles during an orbit. This Vrielmann's result on the constancy of the emission lines in GK Per provides one more evidence of the formation of the lines in the very extended configuration (presumably the wind) surrounding the source. These facts indicate an apparent similarity in observational appearances of red-skewed iron lines in WDs, NSs and BHs. However, the relativistic reflection paradigm does not offer a consistent explanation for the phenomenon across all types of objects. This motivated us to perform the presented study of the iron lines in all three types of compact objects in order to test and compare conventional and alternative theories of the emission line formation.

We extract XMM-*Newton* spectra for WD source GK Per, NS source Ser X-1 and BH source GX 339-4. We analyze the spectra with both relativistic models (DISKLINE and

LAOR) and the wind/outflow models (LT07). In Figures 2-6 we present a comparison of the red-skewed line profile of GK Per and that observed in NS Ser X-1 and BH GX 339-4 sources. While χ^2_{red} statistic value is slightly better for the WINDLINE model in the cases of GK Per and GX 339-4, both models were able to successfully describe the line profiles in all types of objects. Thus the observations of the K_α emission with red-skewed features in CV GK Per suggest that the red skewness of the line cannot be a signature of the GR effects, because the nature of the compact star in GK Per excludes any significant GR effect contribution. If we assume the common origin of the line is WD, NS and BH then there is only one alternative related to the wind (jet) origin of the red-skewed line. On the other hand one can argue that the origin of the red-skewed K_α line in BH and WD sources is different given that in BHs the K_α line is much more red-skewed compared to that in WD (see upper panels of Figs. 2 and 6). The natural question then arises: how one can use observations to choose between these two current paradigms of the origin of K_α line detected from X-ray sources?

In fact, variability properties can arguably provide means to identify conditions in the inner accretion flow and constrain the physical processes governing the formation of the energy spectrum. Let us compare the shortest observable variability time scale seen in PDS of GK Per with a theoretical estimate for the WD emission region. In Figure 7 we present the XMM power spectrum of GK Per related to the XMM photon spectrum shown in Fig. 2. One can see from this Figure that the variability with time scales shorter than 30 s (or in terms of frequency higher than 0.03 Hz) is not present in the data. Provided that the shortest dynamical characteristic time scale $T_{ch} \sim \nu_{ch}^{-1}$ is determined by a ratio of size of WD emission region L_{WD} and acoustic velocity V_A we obtain that $T_{ch} \sim 30\ (L_{WD}/10^9\ \mathrm{cm})/(V_A/3{\times}10^7\ \mathrm{cm})$ s. Here we assume that L_{WD} is of order of WD radius, i.e 10^9 cm and $V_A \sim 10^{-3} \times [kT(\mathrm{keV})]^{1/2}c$. Note the best-fit plasma temperature kT for GK Per spectra is about a few keV (see Table 1) and thus our theoretical expectations perfectly agree with the data. The highest frequency seen in PDS for GK Per is 0.03 Hz ($\sim 1/T_{ch}$). Specifically, the variability shorter than the dynamical time scale (as a ratio L/V_A) is not seen in PDS. In other words *the highest frequency is seen in PDS is directly related to the shortest dynamical scale of the emission region.*

M04c presented a number of arguments against the wind/outflow mechanism of the line production. First, M04c presumed that high optical depth of the wind $\tau_W \gg 1$ can prevent us from seeing the BH detected high QPO frequency (of a few times 100 Hz). In fact, in the observation of BH GX 339-4 we do find a value of τ_W of 4.7. M04c further noted that line emission unaffected by the relativistic regime near BH must occur at radii R_W greater than 100 $R_{\rm S}$ thus M04c argued that the wind model requires the mass outflow rate $\dot{M}_{of}$ to exceed the mass inflow rate $\dot{M}_d$ by at least factor a few. Using the best-fit parameter values of τ_W and β_W for GX 339-4 we find that the inferred $\dot{M}_{of} \sim 6 \times$

$10^{18}A(\tau_W/4.7)(R_W/100R_{\rm S})(\beta/0.0.026)$ g s^{-1}. Here $A = S_W/4\pi R_W^2 \leq 1$ is the dimensionless cross section of the wind and Schwarzschild radius $R_{\rm S} = 3 \times 10^5 m$ cm is calculated for 10 solar mass black hole (i.e. $m = M/M_\odot = 10$). In contrast to the M04c's claim we find that, taking into account uncertainties of parameters entering in $\dot{M}_{out}$ and $\dot{M}_d$, the mass outflow rate $\dot{M}_{out} \lesssim \dot{M}_d$ given that in the high/soft state of BH $\dot{M}_d \sim 3 \times 10^{18}(l/0.2)(m/10)/(\varepsilon/0.1)$ g s^{-1} where $l = L/L_{\rm Edd}$ is the Eddington ratio and $\varepsilon = L/(\dot{M}_d c^2)$ is an efficiency to convert the mass accretion rate to X-ray radiation. Thus, we show that arguments used by M04c to falsify the wind downscattering scenario for iron line production in BH sources do not hold for the presented data from GX 339-4.

Furthermore, according to the M04c's arguments based on the relativistic model, if the GR origin of the line is to prevail for the BH case then the observations of the strongly red-skewed K_α should be accompanied by the detection of short time scale variability in the form of QPO frequencies in the range of 1-10 Hz and higher or broad band Fourier power density components (or even both), because both of them are expected to originate in the innermost part of the emission region.

However, the observational situation in GX 339 is in contradiction to this consequence of the relativistic model. When the strong $K_\alpha-$line was detected (Observation 1 and 2), the simultaneous observations by *RXTE*/PCA showed a typical Comptonization spectra of the high/intermediate soft state with photon index $\Gamma \sim 2.4 - 2.6$ (see Table 3) along with a low variability, noisy (forest-type) PDS with no QPO features and no broken power-law continuum (see Fig. 5, *right upper and middle panels*). On the other hand, during the XMM observation on 2003 March 8 (Observation 3) when the iron line was weak the *RXTE* observations showed a PDS with a clean feature of a broken power-law (white-red noise component) with a break frequency at about 2 Hz and QPOs with centroid frequencies of 8 and 16 Hz. In the next two subsections we show that the suppressed high frequency variability can be readily explained by the presence of the optically thick wind outflow.

As a result we find that both relativistic and wind/outflow model are able to successfully fit the data on iron emission lines from compact X-ray sources. Even formally applied for the WD case relativistic models satisfactory fit the data. Therefore, red-shift itself is not a reliable signature of the GR effects. Relativistic reflection scenario cannot explain the lack of variability of the line observed in CVs (Vrielmann et al. 2005) and is in contradiction with the observation of the suppressed high frequency variability during the "line"-state in BH source GX 339-4. Hence, considered in the context of variability properties the wind/outflow scenario emerges as a favorable explanation of red-skewed lines in accreting X-ray binaries.

3.1. The wind effect on the resulting power spectrum

In the presence of the optically thick outflow the emergent timing signal $W(t)$ is a convolution of X-ray timing signal originated in the innermost part of the source $X(t)$ and the outflow transformation function due to photon scattering $\varphi(t)$ see (see Titarchuk et al. 2007):

$$W(t) = \int_0^t X(t')\varphi(t-t')dt'. \tag{1}$$

The response of any bounded configuration due to photon scattering is exponential [see e.g. Sunyaev & Titarchuk (1980) and Laurent & Titarchuk (2007)] . Thus

$$\varphi(t) = A\exp(-t/t_0) \tag{2}$$

where $t_0 \sim \tau_W L_W/c$ is the outflow (wind) scattering (photon diffusion) time scale, τ_W is the outflow Thomson optical depth, L_W is the scattering wind size and $A = 1/t_0$ is the normalization constant ($\int_0^\infty X(t)dt = 1$).

The resulting power spectrum $||F_W(\omega)||^2$ is a product of the power spectra of $\varphi(t)$ and $X(t)$, namely

$$||F_W(\omega)||^2 = ||F_X(\omega)||^2||F_\varphi(\omega)||^2 \tag{3}$$

where $F_W(\omega),\ F_X(\omega),\ F_\varphi(\omega)$ are Fourier transforms of $W(t),\ X(t),\ \varphi(t)$ respectively, and $\omega = 2\pi\nu$ is a rotational frequency.

The power spectrum of $\varphi(t)$ is a centered Lorentzian

$$||F_\varphi(\omega)||^2 = \frac{(1/t_0)^2}{\omega^2 + (1/t_0)^2}. \tag{4}$$

If for example, X-ray signal $X(t)$ can be presented a quasi-periodic (QPO) oscillations related to the frequency $\omega_* = 2\pi\nu_*$ then the corresponding PDS is a Lorentzian of the form:

$$||F_X(\omega)||^2 = \frac{C_N}{(\omega-\omega_*^2) + (\hat{\Gamma}/2)^2}. \tag{5}$$

where $\hat{\Gamma}$ is a FWHM and C_N is the normalization constant of the QPO PDS.

In Figure 8 we present the plot of power spectra $||F_X(2\pi\nu)||^2$ and $||F_\varphi(2\pi\nu)||^2$ along with the resulting PDS $||F_W(2\pi\nu)||^2$. One can see from upper panel of Fig. 8 that when ν_* and $1/(2\pi t_0)$, the characteristic frequencies of X-PDS and $\varphi-$PDS respectively [or characteristic time scales $1/(2\pi\nu_*)$ and t_0], are comparable then the PDS intrinsic features of X-ray signal originated in the innermost part of the source is unaffected by photon scattering in the wind.

In the opposite case when $\nu_* >> 1/(2\pi t_0)$ the QPO feature of X-PDS is completely washed out, see black line in lower panel of Fig. 8.

The similar washing out effect can be seen in the general case when X-PDS is presented a superposition of white-red noise (broken power law) and QPO Lorentzians. (see e.g. Titarchuk et al. 2007). All power related to frequencies $\nu \gg 1/(2\pi t_0)$ are suppressed due photon scattering in the wind.

3.2. Forest type of PDS in the "line" state

The observational correlation of the strong line and the forest-type power spectrum gives a strong support for the wind (outflow) origin of the line in BH at least in GX 339-4. For a particular source the presence of a strongly red-skewed iron line along with the forest-type PDS in the data can be considered an observational signature of wind (or wide open jet) [see above cases of GK Per and GX 339-4, (Observation 2)].

Namely, when the powerful wind occurs, presumably as a consequence of high mass rate in the source, the wind is illuminated by the emission of the innermost part of BH source to produce the highly red-skewed iron line but on the other hand any variability of X-ray innermost emission region is suppressed by the wind given its extension. For the characteristic size of the wind $L_W \gtrsim 10^3 R_{\rm S}$, the wind optical depth of 4.7 and 10 solar masses BH, i.e. $m = M_{BH}/M_\odot = 10$, the photon scattering time in the wind (see Eq. 2)

$$t_0 \underset{\sim}{>} 0.5 \left(\frac{\tau_W}{4.7}\right) \left[\frac{L_W}{10^3 (m/10)(R_{\rm S}/3\times 10^6 \text{ cm})}\right] \frac{3\times 10^{10} \text{ cm s}^{-1}}{c} \text{ s.} \quad (6)$$

Thus according to the above inequality all frequencies higher than

$$\nu > 1/(2\pi t_0) \sim 0.3 \left(\frac{\tau_W}{4.7}\right)^{-1} \left[\frac{L_W}{10^3 (m/10)(R_{\rm S}/3\times 10^6 \text{ cm})}\right]^{-1} \left(\frac{3\times 10^{10} \text{ cm s}^{-1}}{c}\right)^{-1} \text{ Hz} \quad (7)$$

are smeared (suppressed) due the photon scattering in the wind. This effect of the wind photon scattering is presumably seen in the PDS in a so called "line state" when the strong line is observed in Observations 1 and 2 of BH GX 339-4 (see middle and top panels of Fig. 5).

3.3. Variability of X-ray emission, line appearances and so called "reflection" effect

As we show above the detection of the strong K_α line along with a weak variability of X-ray can be an observational signature of presence of the powerful wind in the system (see Fig. 5, upper and middle panels). On the other hand one may also expect the weak line along with high variability of X-ray emission of the source as a signature of the weak wind (see Fig. 5, low panels). Thus a noticeable fraction of X-ray variability presumably originated in the innermost part of the source $\exp(-\tau_W)$ is unaffected by the wind and passes through the wind if $\tau_W \lesssim 1$. Indeed, in Observation 3 we probably see an optically thin wind which signatures are a weak line having almost Gaussian profile and noticeable high variability. LT07 considered only the line scattered component because the line profile of the direct component is very sensitive to the wind geometry and to the position of the Earth observer.

3.3.1. Formation of direct component of the wind line

The direct component of the windline model may be fitted by the Gaussian line profile if the wind is symmetric with respect to the Earth observer (see an example in Appendix B). In the opposite case the line profile can be asymmetric, blue-skewed or red-skewed. The wind line profile of the optically thin wind is described by the direct component only. In this case strong variability of the central engine is unaffected because the attenuation of this signal is $\exp(-\tau_W) \sim 1$. LT07 showed that the source of K_α in the wind is mostly located in the narrow shell near the innermost part of the wind (see details in LT04 and LT07). One can assume that K_α photons are emitted isotropically by a given element of the wind shell of radius r and the local line profile is described by Gaussian

$$I_L(E, r, \mu) = \frac{1}{\pi^{1/2}\Delta E_{\rm D}} \exp\left\{-\frac{[E - E_0(1 + \beta_W(r)\mu)]^2}{\Delta E_{\rm D}}\right\} \tag{8}$$

where $\Delta E_{\rm D} = E_0(kT_W/m_{Fe})^{1/2}/c$ is the intrinsic Doppler width of the line which is very small, i.e. $\Delta E_{\rm D} = 1.3 \times 10^{-4}(kT_W/1\ {\rm keV})^{1/2}E_0$, $\mu = \cos\theta$ and θ is angle between the velocity vector $\mathbf{V}_W$ and the vector the line of sight $\mathbf{n}_{ert}$, i.e $\mu = (\mathbf{n}_W \cdot \mathbf{n}_{ert})$, $\mathbf{n}_W = \mathbf{V}_W/V_W$ is unit vector of $\mathbf{V}_W$. This line profile can be derived using the bulk local Maxwellian distribution for atom (iron) velocities (Titarchuk & Zannias 1998) and Doppler effect [see Rybicki & Lightman (1979) for details of this derivation for the pure thermal motion].

The line flux emitted by the wind shell detected by the Earth observed $F_L(E)$ is a sum (integral) of a projection of the line intensity of each element of the wind shell to the line of

sight. Namely,

$$F_L(E) = \frac{1}{E_0}\int_{R_{in}}^{\infty}\frac{F(r)r^2}{\beta_W(r)}dr\int_0^{2\pi}d\varphi\times$$
$$[\beta_W(r)E_0]\left[\int_{\mu_{1,+}}^{\mu_{2,+}}|\mu|I_L(E,r,\mu)d\mu' + \int_{\mu_{2,-}}^{\mu_{1,-}}|\mu|I_L(E,r,\mu)d\mu'\right] \quad (9)$$

where $F(r)$ is the line emissivity at r, $\mu = \mathbf{n}_W\cdot\mathbf{n}_{ert} = \mu'\mu_0+(1-\mu'^2)^{1/2}(1-\mu_0^2)^{1/2}\cos(\varphi-\varphi_0)$, $\mathbf{n}_W = \{(1-\mu'^2)^{1/2}\cos\varphi, (1-\mu'^2)^{1/2}\sin\varphi, \mu'\}$, $\mathbf{n}_{ert} = \{(1-\mu_0^2)^{1/2}\cos\varphi_0, (1-\mu_0^2)^{1/2}\sin\varphi_0, \mu_0\}$ and $\mu_{1,+}$, $\mu_{2,+}$ and $\mu_{1,-}$, $\mu_{2,-}$ are cosines of angles of toward and outward wind cones, for which $\mathbf{n}_W\cdot\mathbf{n}_{ert} > 0$ and $\mathbf{n}_W\cdot\mathbf{n}_{ert} < 0$ respectively. For the symmetric case $\mu = \mu'$, $-\mu_{1,-} = \mu_{1,+} \geq 0$ and $-\mu_{2,-} = \mu_{2,+} > 0$.

In Appendix B we show how one can obtain the Gaussian-like profile of the wind line from the spherical wind (see Fig. 9). The general case of the wind geometry and relative position of the Earth observer with respect to the wind will be presented elsewhere. The Earth observer could detect the line profile if she/he could spatially resolve a contribution of each particular spherical shell of the wind. We can use the steepest descend method, given that $\Delta E_{\rm D} \ll E_0$, to calculate the internal integral I_{in} of Eq. (9). We obtain that the profile of the line coming from a given spherical shell (see Fig. 9)

$$\mathcal{I}(E,r) = [\beta_W(r)E_0]I_{in} = \begin{cases} \frac{|E-E_0|}{\beta_W(r)E_0} & \text{for } |E-E_0| \leq \beta_W(r)E_0; \\ 0 & \text{for } |E-E_0| \geq \beta_W(r)E_0. \end{cases} \quad (10)$$

is a broken power-law with the center at $E = E_0$. The resulting direct component of the line profile is a sum of the contribution of each of the shells, i.e. the sum of the product of the line emissivity and the broken power-line profile $\mathcal{I}(E,r)$ (see Eq. B1). Note if the wind is not symmetric with respect to the observer then the line profile is also asymmetric with respect to E_0 (the line rest-frame energy).

Thus one can see that the line profile can be presented by the Gaussian-like shape in the case of optically thin symmetric wind. Moreover we show in Appendix B that the inferred Gaussian width σ_{ga} can be related to the mean dimensionless bulk velocity $\beta_{mn} \sim \beta_W \sim \sigma_{ga}/E_0$. We can infer the wind velocity $V_W \sim 0.1$c for Observation 3 using this relation for β_W and the inferred values of $\sigma_{ga} \sim 0.69$ keV and $E_L = E_0 \sim 6.4$ keV (see Table 3). The wind velocity 0.1c is consistent with an optically thin wind in the case of Observation 3. Indeed if the mass outflow does not change through Observations 1-3 one can estimate, using the continuity equation for the wind, that τ_W should be inversely proportional to V_W and then $\tau_{W,3} \sim (V_{W,2}/V_{W,3})\tau_{W,2} \sim 1$. Such a low value of $\tau_{W,3}$ is consistent with the presence of high variability in Observation 3 because, at least, 1/3 of variability of the central engine can be directly seen and unaffected by the wind.

3.3.2. On the "relativistic" line picture

One can ask a fair question: could be that the wind line model holds in some cases (e.g., High Soft State and Soft Intermediate State), whereas the relativistic line picture holds elsewhere (Hard Intermediate State)? The suggested relativistic line is a combined effect of the presence of the cold target (disk) in the innermost part of the source and high visibility of the source innermost part. The high visibility is, indeed, confirmed by some particular observations of BH sources when high frequencies QPOs are seen in their power spectra up to 200 Hz [see Remillard & McClintock (2006)]. However the presence of cold unionized material in the innermost part of the source is strongly ruled out by ionization state of this region. LT04 demonstrated that the innermost part of the disk is completely ionized. They used extensive calculations of interaction of X-ray hard radiation emanated from the central region with surrounding plasma.

The relativistic line paradigm is also related to the reflection problem of X-ray radiation. In fact, in our fits of the GX 339-4 spectra, we find essentially no need for reflection but it is not by chance that the reflection bump is not seen in the data. We remind a reader that the reflection bump is a combined effect of downscattering hard photons of the incident spectrum and photoelectric absorption of photons which energies are lower than 10 keV (Basko et al. 1974). It is impossible to form a downscattering bump when the spectral continuum is very soft, like in the GX 339-4 spectra presented here, for which photon indices $\Gamma = \alpha + 1$ are about 2.5 (see Table 4). In fact, LT07 demonstrated using analytical consideration and Monte Carlo simulations that for $\Gamma > 2$ there is *no* bump in the reflection spectrum, due to downscattering accumulation of photons from high energy tail of the incident spectrum. In other words the incident spectrum is too steep in order to have enough photons to form the downscattering bump in the reflection spectrum. On the other hand as we argue above the innermost part of the disk is completely ionized and there is no "cold" disk there. Note the subtended angle of the hard X-ray emission emanated from the source central part is highest for the disk located in the same central area. Therefore we can conclude that the reflection bump cannot be formed, in the innermost part of the disk, as a result of the photo-electric absorption and photon dowscattering of hard X-ray photons.

4. Conclusions

We utilize XMM-*Newton* data from Epic-PN Camera to study the red-skewed iron lines in GK Per, Ser X-1 and GX 339-4 as representatives of WD, NS and BH X-ray binary sources respectively. We analyze the iron line profiles in terms of both relativistic reflection and wind outflow models. We also use simultaneous *RXTE* data to obtain information on high energy

part of the spectrum and high frequency variability for GX 339-4.

We base our conclusions on the following facts: i. all three types of accretion compact objects show red-skewed iron K_α lines, ii. outflow is a common phenomenon for CVs, NSs and BHs, iii. we demonstrate the ability for the wind model to describe the asymmetric shapes of the lines detected from CV, NS and BH sources and iv. we show the observational correlation of the strong line and forest-type power spectrum in BH. The lack of high frequency variability weakens the red-skewed line connection with high frequency QPOs and strengthens its connection to a wind/outflow phenomena. We should also point out whereas a lack of high frequency variability could be counted as observational support for the wind model however it cannot be counted as observational evidence against the relativistic line model. At least without knowing what the underlying variability spectrum should be. Moreover, we also point out that Gaussian-like profiles of relatively narrow iron lines, $\sigma_{ga} \sim \beta_W E_L \ll E_L$, can be a direct line component coming from optically thin wind.

These points and the difficulty for the GR effects to account for red wings in the iron lines observed in CV sources favor a wind origin of the red-skewed line profile of K_α iron emission in all these sources.

The authors acknowledge the productive discussion the paper content with Martin Laming, Michael Wolff, Kent Wood, Marat Gilfanov, Filippo Frontera, Remo Ruffini, Vadim Arefiev, Elena Seifina and Mike Nowak. We are very grateful to the referee for his useful comments and suggestions which significantly improve the paper presentation.

A. The Comptonization Green's function as a Generic Green's function for photon upscattering off energetic electrons of plasma cloud and for capital gain due to investment

Drâgulescu & Yakovenko (2001), hereafter DY01, present the data on wealth and income distributions in the United Kingdom (UK) , as well as on the income distributions in the individual states of the USA. They found that the great majority of wealth and income distribution (95%) is described by an exponential distribution, whereas the high-end tail follows a power law (see Fig. 1-3 in DY01). In fact, the exponential gross income distribution is similar to blackbody (BB)-like distribution $B_{ph}(E)$ for photons emerged from the optical thick configurations such either a disk or a stellar atmosphere. Actually to fit the data DY01 used the exponential law $P_{maj}(w) \propto \exp(-w/W)$ where $P(w)$ stands for probability density to have a wealth $\mathcal{W}$ between w and $w + dw$ and W is a characteristic (mean) wealth for a given data selection (for either population of USA or UK). The mean wealth

W has a full analogy with BB temperature. The exponential law, also known in physics as the Boltzmann−Gibbs distribution, is characteristic for a conserved variable, such as energy. DY01 argued that, because money (cash) is conserved, the probability distribution of money should be exponential. Wealth can increase or decrease by itself, but money can only be transferred from one agent to another. So, wealth is not conserved, whereas money is.

Below we show the photon distribution due upscattering of soft (seed) photons off energetic electrons as a power law is similar to the capital gain distribution due to investment, for example in a stock market. We denote the intensity of the injected monochromatic soft photons of energy E_0 and gaining energy due to scattering in the Compton cloud as $I(E_0, E)$ and $N_{ph} = I(E_0, E)/E$. As for the capital gain due to investment $M(w_0, w)$ and $P(w_0, w) = M(w_0, w)/w$. Because the derivation is similar for photon and wealth distributions we present this for $N_{ph}(E)$ and through the derivation we draw a parallel between terminology for photons and capital gains. Note that in the system, disk+Compton Cloud only some fraction of seed (disk) photons f is affected by upscattering off CC energetic electrons but (1-f) fraction of seed photons comes directly to the observer. The same is true for the wealth distribution. Only some fraction of money f belonging to $N_{maj}(w)$−part is invested into either stock market or big business. The (1-f)-fraction of the majority of population does not contribute into this business activity.

The intensity (amount of capital gain) of the injected soft photons of energy E_0 (or investment of amount w_0) undergoing k scatterings in the Compton cloud is

$$I(E_0, k) \propto p^k \tag{A1}$$

where p is average probability of photon scattering in the CC , or in the case of capital gain is average probability of success due to investment. Note that as in the photon case the probability of photon scattering p is directly related to mean number of scatterings (or successful investments)

$$\mathcal{N}_{sc} = \sum_{k=1}^{\infty} k p^k q = p/(1-p) \tag{A2}$$

where $q = 1 - p$ is the probability of the photon escape from the CC or that of the failure in the investment case. Thus, using Eq. (A2), we obtain

$$p = 1 - 1/(\mathcal{N}_{sc} + 1). \tag{A3}$$

Because the average photon energy (money) change per scattering (investment) $< \Delta E >= \eta E$ (where $\eta > 0$ for the upscattering case or successful investment), the injected photon energy after k scatterings E is

$$E = (1 + \eta)^k E_0 \tag{A4}$$

For simplicity of presentation here we drop subscript k for the value of photon energy E_k after k-scattering (or for capital gain after k successful investments).

The combination of Eqs. (A1), (A4) yields that the emergent upscattering spectrum of the soft photon of energy E_0 in the bounded Compton cloud is a power law

$$I(E_0, E) \propto \left(\frac{E}{E_0}\right)^{-\alpha} \tag{A5}$$

which index

$$\alpha = \frac{\ln(1/p)}{\ln(1+\eta)}. \tag{A6}$$

Using Eq. (A3) we can reduce Eq. (A6) to

$$\alpha \approx (\eta \mathcal{N}_{sc})^{-1} = Y^{-1}. \tag{A7}$$

for $\mathcal{N}_{sc} \gg 1$ and $\eta \ll 1$. Thus the photon distribution over E [or probability of the capital distribution of the population over w, $N(w_0, w)$] is

$$N_{ph}(E_0, E) = I(E_0, E)/E \propto \left(\frac{E}{E_0}\right)^{-\Gamma} \tag{A8}$$

where $\Gamma = \alpha + 1$. In order to obtain the upscattering (capital gain) component of the resulting photon (capital) distribution $N_{ph,res}(E)$ we should convolve the upscattering photon Green's funcition $N_{ph}(E_0, E)$ [or $N(w_0, w)$] with some fraction f of a seed photon distribution $B_{ph}(E_0)$ [or with some fraction f of the majority exponential capital distribution $P_{maj}(w_0)$ in the case of gross income distribution]. Then we add the direct component of the seed photons unaffected by upscattering $(1-f)B(E)$ with the upscattering photon component, i.e.

$$N_{ph,res}(E) = (1-f)B_{ph}(E) + f\int_0^\infty N_{ph}(E_0, E)B_{ph}(E_0)dE_0. \tag{A9}$$

It is easy to show that the shape of the distribution $N_{ph,res}(E)$ [or $N_{res}(w)$] is an exponential up to some energy and then it follows by power law to high-end of the spectrum. Thus we can conclude that the photon Comptonization spectrum as a convolution of the Green's function (as a broken power law) with the seed photon spectrum (BMC model) is applicable to describe the resulting shape of the USA and UK measured wealth distributions.

B. The direct line component

As it follows from Eqs. (9-10) the resulting direct component of the line profile is

$$F_L(E) = 2\pi x \int_{R_{min}}^\infty \frac{F(r)r^2 dr}{\beta_W^2(r)} \tag{B1}$$

where $x = |E - E_0|/E_0$ and R_{min} ($> R_{in}$) is determined by condition that

$$\frac{xf(R_{min})}{\beta_W^2(R_{min})} = \frac{f(R_{min})}{\beta_W(R_{min})} \tag{B2}$$

which identical to

$$x = \beta_W(R_{min}). \tag{B3}$$

This equation can be solved analytically if we assume that

$$\beta_W(r) = a(r - R_{in})^\alpha \tag{B4}$$

where $\alpha > 0$.

We can introduce a new integration variable $y = R - R_{in}$ and rewrite Eq. (B1) using Eq. (B4) as follows

$$F_L(E) = 2\pi \frac{x}{a} \int_{(x/a)^{1/\alpha}}^{\infty} \frac{F(R_{in}+y)(R_{in}+y)^2}{\beta_W(y)} \frac{dy}{y^\alpha} \tag{B5}$$

Because the line emissivity decays exponentially with respect to y (see LT04 and LT07) we can also assume that

$$\mathcal{W}(y) = \frac{(R_{in}+y)^2 F(R_{in}+y)}{\beta_W(y)} = C_0(R_{in}) \frac{1}{y} \exp(-ba^2 y^{2\alpha}) \tag{B6}$$

where $b > 0$. With this assumption regarding function $F(r)$ the integral in Eq. (B5) diverges at the lower limit of integration and thus we obtain the Gaussian-like profile.

$$F_L(E) \propto \exp(-bx^2). \tag{B7}$$

One can ask a natural question how the coefficient b of exponential of Eq. (B6) is related to the mean value of the dimensionless bulk velocity β_{mn} which by definition is

$$\beta_{mn} = \frac{\int_0^\infty \beta_W(y)\mathcal{F}(y)(y)dy}{\int_0^\infty \mathcal{F}(y)dy}. \tag{B8}$$

where $\mathcal{F}(y) = \beta_W(y)\mathcal{W}(y)$. Using Eqs. (B4, B6) we can rewrite Eq. (B8) as follows:

$$\beta_{mn} = \frac{a^2 \int_0^\infty y^{2\alpha-1} \exp(-ba^2 y^{2\alpha})dy}{a \int_0^\infty y^{\alpha-1} \exp(-ba^2 y^{2\alpha})dy}. \tag{B9}$$

To calculate integrals in Eq. (B9) we introduce new integration variables $t = a^2 b y^{2\alpha}$ and $z = ab^{1/2} y^\alpha$, for the numerator and denominator respectively. Then we obtain that

$$\beta_{mn} = D_0 b^{-1/2} \tag{B10}$$

where the numerical factor

$$D_0 = \frac{\alpha - 1}{\pi^{1/2}(\alpha - 1/2)} \lesssim 1 \tag{B11}$$

is of order of one if $\alpha > 1$.

REFERENCES

Drâgulescu, A. & Yakovenko, V.M. 2001, Physica A, 229, 213

Basko, M. M., Sunyaev & Titarchuk, L. G. 1974, A&A , 31, 249

Bhattacharyya, S. & Strohmayer, T.E. 2007, ApJ, 614, L103 (BhS07)

Cackett, E. M., et al. 2008, ApJ, 674, 415

Fabian, A.C., Rees, M.J., Stella, L., & White, N. 1989, MNRAS 238, 729

Hellier, C. & Mukai, K. 2004, MNRAS, 352, 1037 (HM04)

Homan, J., & Belloni, T. 2005, Ap&SS, 300, 107

Hua, X-M. & Titarchuk, L. 1995, ApJ, 449, 188

Laming, J.M. & Titarchuk, L. 2004, ApJ, 615, L121 (LT04)

Laor, A. 1991, ApJ, 376, 90

Laurent, P. & Titarchuk, L. 2007, ApJ, 656, 1056 (LT07)

McNamara, A. L., Kuncic, Z., Wu, K., Galloway, D. K., & Cullen, J. G. 2008, MNRAS, 383, 962

Miller, J. M. 2007, ARAA, 45, 441 (M07)

Miller, J. et al. 2004c, *in Proceedings of 10th Marcel Grossmann Meeting, Ed. R. Ruffini*, astro-ph/0402101

Miller, J. M. et al. 2004b, ApJ, 606, L131(M04b)

Miller, J. M. et al. 2004c, ApJ, 601, 450 (M04c)

Miniuti, G., Fabian, A.C. & Miller, J. M. 2004, ApJ, MNRAS, 351, 466

Montanari, E., Titarchuk, L. & Frontera, F. 2009, ApJ, in press (arXiv:0810.5720)

Rybicki, G. B., & Lightman, A. P. 1979, Radiative Processes in Astrophysics (New York, Wiley-Interscience)

Remillard, R. A., & McClintock, J. E. 2006, ARA&A, 44, 49

Reynolds, C. S. & Nowak, M. A. 2003, Physics Reports, 377, 389

Sunyaev, R.A. & Titarchuk, L.G. 1980, A&A, 86, 121

Tanaka, Y., et al. 1995, Nature, 375, 659

Titarchuk, L.G. 1994, ApJ, 434, 570

Titarchuk, L., Kazanas, D. & Becker, P. 2003, ApJ, 598, 411

Titarchuk, L., Shaposhnikov, N. & Arefiev, V. 2007, ApJ, 660, 556

Titarchuk, L., & Zannias, T. 1998, ApJ, 493, 863

Vrielmann, S., Ness, J.-U. & Schmidt, J.H.M.M. 2005, A&A, 439, 287

Warner, B. 1995, Cataclysmic Variables (Cambridge: Cambridge Univ. Press)

Wilms, J. et al. 2001, MNRAS, 328, L27

Table 1. Best-fit Parameters for the *XMM-Newton* Spectrum of CV GK Per

Component	Parameter	LAOR	DISKLINE	WINDLINE
EDGE	E_{edge} (keV)	7.11±0.02	7.09±0.03	7.09±0.04
	τ_{max}	0.35±0.03	0.36±0.02	0.23±0.03
WABS	N_H (cm^2)	1.5±0.3	1.2±0.1	2.0±1.0
BBODY	T_{bb}, keV	0.16±0.04	0.15±0.01	0.12±0.01
COMPTT	T_0 (keV)	$0.9^{+0.5}_{-0.1}$	1.18±0.01	1.05±0.57
	kT_e (keV)	3.40±0.07	3.4±0.3	5.3±0.5
	τ_e	32.3±4.5	27.0±0.2	20.9±1.8
K_α line[a]	E_L (keV)	6.49±0.02	6.46±0.03	6.48±0.05
	β_L	2.14±0.16	2.4±0.2	-
	R_{in} (R_G)	12.5±2.5	22±3	-
	R_{out} (R_G)	400[f]	1000[f]	-
	i_L (deg)	4±4	13.5±1.5	-
	τ_W	-	-	1.46±0.06
	$\beta_W = V_W/c$	-	-	(0.71±0.06)×10^{-2}
	kT_W (keV)	-	-	0.97±0.06
	EW_L, eV.....	197±15	176±30	641±90
Fit quality	χ^2_{red} (χ^2/N_{dof})	1.19 (1114.6/934)	1.20 (1123/934)	1.15 (1071/934)

[a]Model is specified by the name at the top of a column

[f]Parameter fixed

Table 2. Best-fit Parameters for the *XMM-Newton* Spectrum of NS Serpens X-1

Component	Parameter	LAOR[a]	DISKLINE	WINDLINE
WABS	N_H (cm^2)	0.32±0.02	0.35±0.01	0.37±0.02
BBODY	T_{bb} (keV)	0.29±0.01	0.27±0.01	0.25±0.01
COMPTT	T_0 (keV)	0.55±0.02	0.518±0.002	0.50±0.02
	kT_e (keV)	3.01±0.01	2.91±0.04	2.91±0.05
	τ_e	13.1±0.1	13.4±0.1	13.4±0.2
K_α line	E_L (keV)	6.57±0.02	6.57±0.04	6.67±0.01
	β_L	1.67±0.16	2.12±0.08	-
	R_{in} (R_G)	1.23[b]	6.0[b]	-
	R_{out} (R_G)	400[f]	1000[f]	-
	i_L (deg)	65±3	62±8	-
	τ_W	-	-	1.6±0.1
	$\beta_W = V_W/c$	-	-	(1.5±0.1)×10^{-2}
	kT_W (keV)	-	-	1.21±0.06
	χ^2_{red} (χ^2/N_{dof})	1.15 (2292/1991)	1.13 (2245/1991)	1.14 (2264/1991)

[a]Model is specified by the name at the top of a column

[b]Parameter value pegged into the lower limit set by the model

[f]Parameter fixed

Table 3. Gaussian Fit for the Iron Line for GX 399-4 observations in Different BH States

Obs.	Date	BH state[a]	Γ ($\alpha_{BMC}+1$)	f_C[b]	σ_{ga} (keV)	EW[c] (eV)	χ^2_{red} (χ^2/N_{dof})
1	24/08/2002*	SIMS	2.37±0.02	0.22±0.01	1.29±0.07	233±40	1.19 (2318/1941)
2	29/09/2002**	HSS	2.54±0.01	0.30±0.01	1.24±0.02	684±20	1.27 (2469/1941)
3	08/03/2003***	HIMS	2.17±0.02	0.38±0.01	0.69±0.11	167±55	1.03 (1997/1945)

[a]BH states: SIMS - soft intermediate state, HIMS - hard intermediate state, HSS - high soft state (see Homan & Belloni 2005, for details).

[b]$f_C = A/(1+A)$.

[c]The centroid energy of the Gaussian was fixed at 6.4 keV.

*XMM/*RXTE* Obs ID: 0093562701/70130-01-01-00

**XMM/*RXTE* Obs ID: 0156760101/70130-01-02-00

***XMM/*RXTE* Obs ID: 0148220201/50117-01-03-00

Table 4. Best-fit Parameters for the XMM/*RXTE* Spectrum of BH GX 339-4 on September 29, 2002 (Observation 2)

Component	Parameter	LAOR[a]	DISKLINE	WINDLINE
WABS	N_H (cm^2)	0.354±0.005	0.356±0.005	0.365±0.006
BBODY	T_{bb} (keV)	0.332±0.003	0.331±0.003	0.319±0.004
BMC	kT (keV)	0.679±0.003	0.678±0.002	0.662±0.004
	α	1.55±0.01	1.60±0.01	1.44±0.02
	log(A)	-0.74±0.01	-0.75±0.01	-0.91±0.01
K$_\alpha$ line	E_L (keV)	6.4[b]	6.4[b]	6.60±0.15
	β_L	1.62±0.04	2.40±0.05	-
	R_{in} (R_G)	1.23[b]	6.0[b]	-
	R_{out} (R_G)	400[f]	1000[f]	-
	i_L (deg)	80[c]	80[c]	-
	τ_W	-	-	4.9±0.2
	$\beta_W = V_W/c$	-	-	(2.47±0.02)×10^{-2}
	kT_W (keV)	-	-	1.06±0.02
	χ^2_{red} (χ^2/N_{dof})	1.33 (2573/1937)	1.34 (2596/1937)	1.24 (2401/1937)

[a]Model is specified by the name at the top of a column

[b]Parameter value pegged into the lower limit set by the model

[c]Parameter value pegged into the upper limit set by the model

[f]Parameter fixed

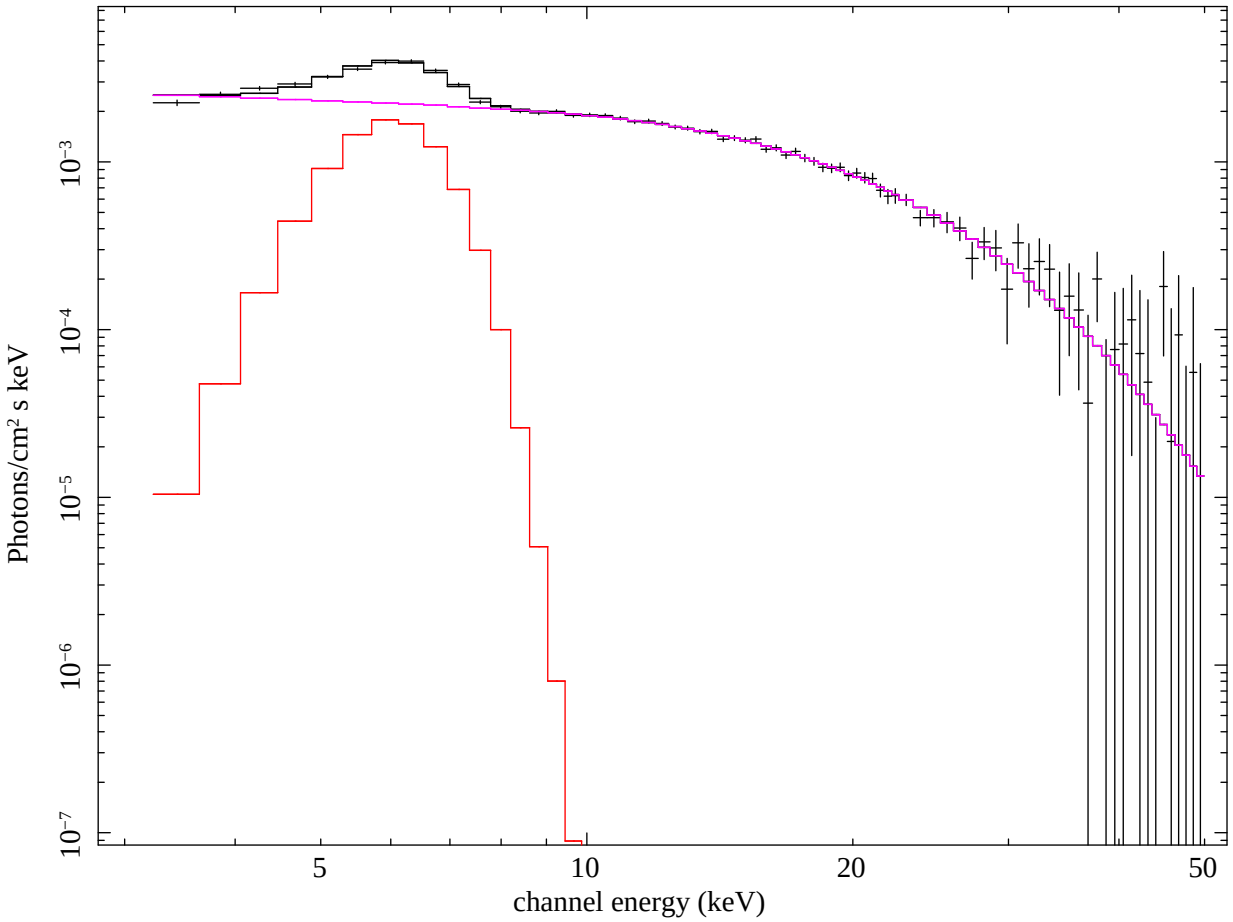

Fig. 1.— The *RXTE* observation of GK Per The data (error bars) vs model (solid line). Here we have used the best-fit model WABS∗(COMPTT+GAUSSIAN).

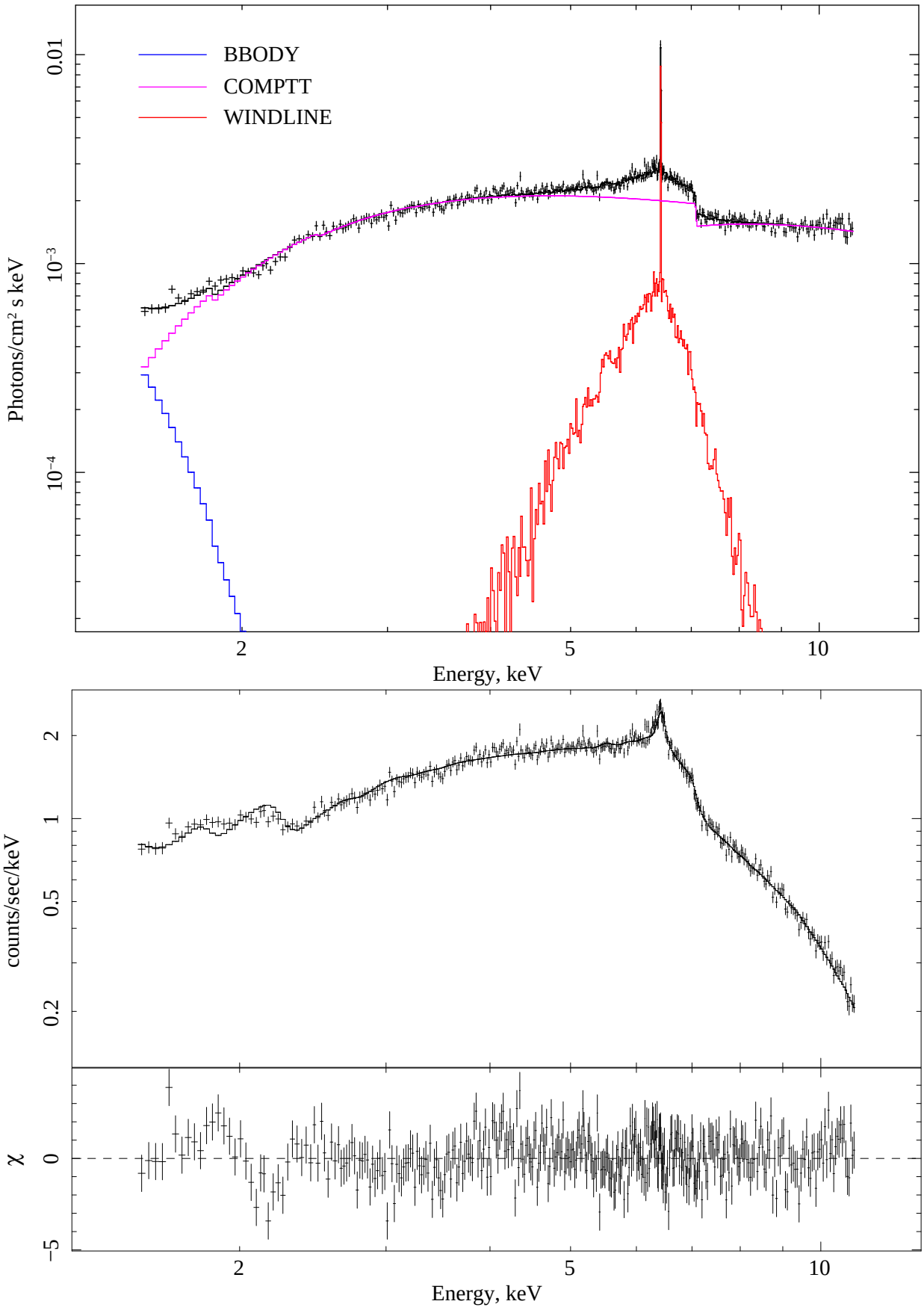

Fig. 2.— The XMM-*Newton* observation of GK Per (rev. 412) The data

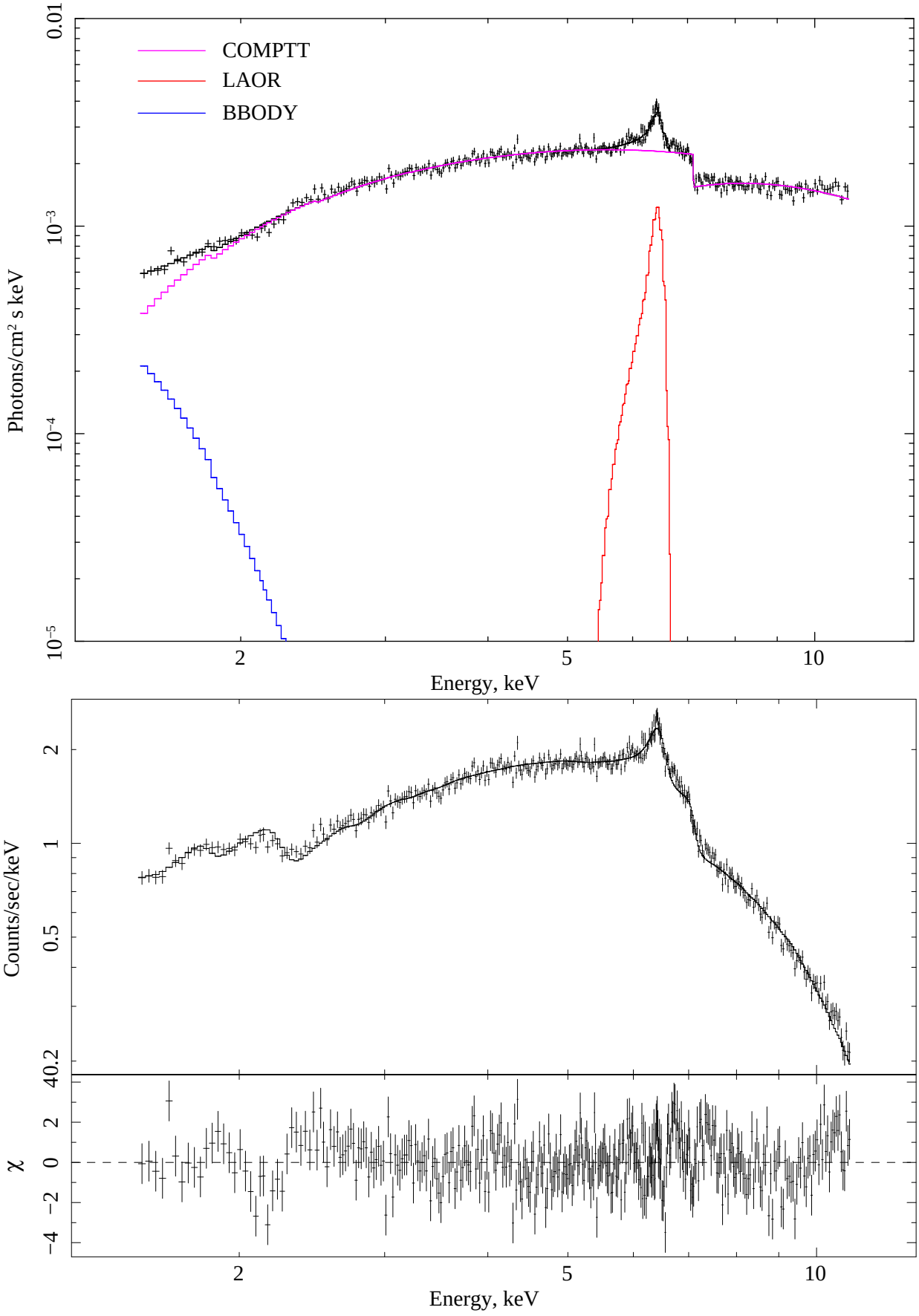
COMPTT
LAOR
BBODY
Photons/cm² s keV
0.01
10⁻³
10⁻⁴
10⁻⁵
2
5
10
Energy, keV
Counts/sec/keV
2
1
0.5
40.2
χ
2
0
−2
−4
2
5
10
Energy, keV

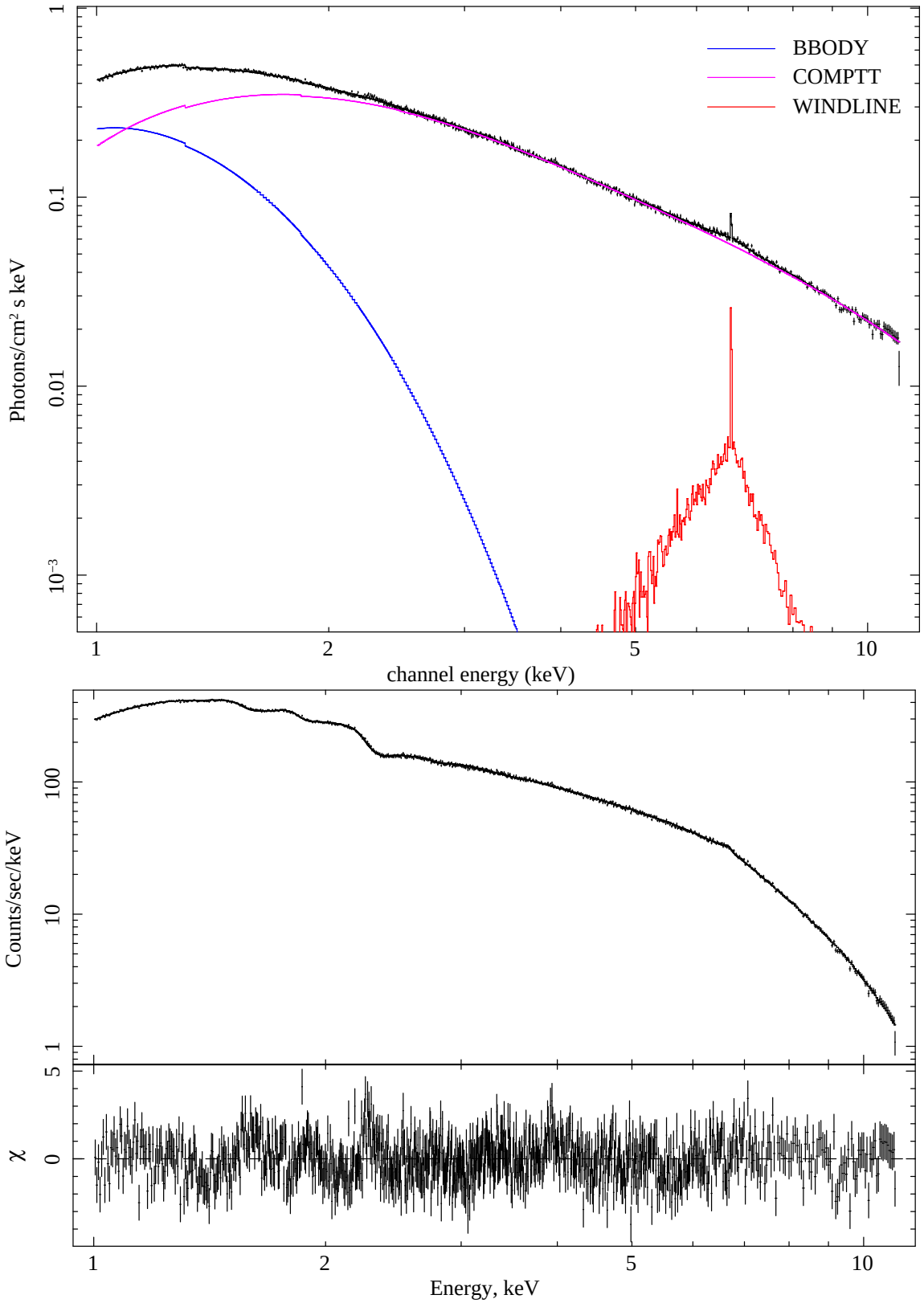

Fig. 4.— The XMM-*Newton* observation of Ser X-1 (XMM rev. 785) The upper panel shows the data (error bars), model (solid line). Here we have used the best-fit XSPEC model WABS∗(COMPTT+BBODY+WINDLINE) (see Table 2). The lower panel shows the count spectrum along the residual of the data vs model in units of $\chi = (\text{data} - \text{model})/\sigma$.

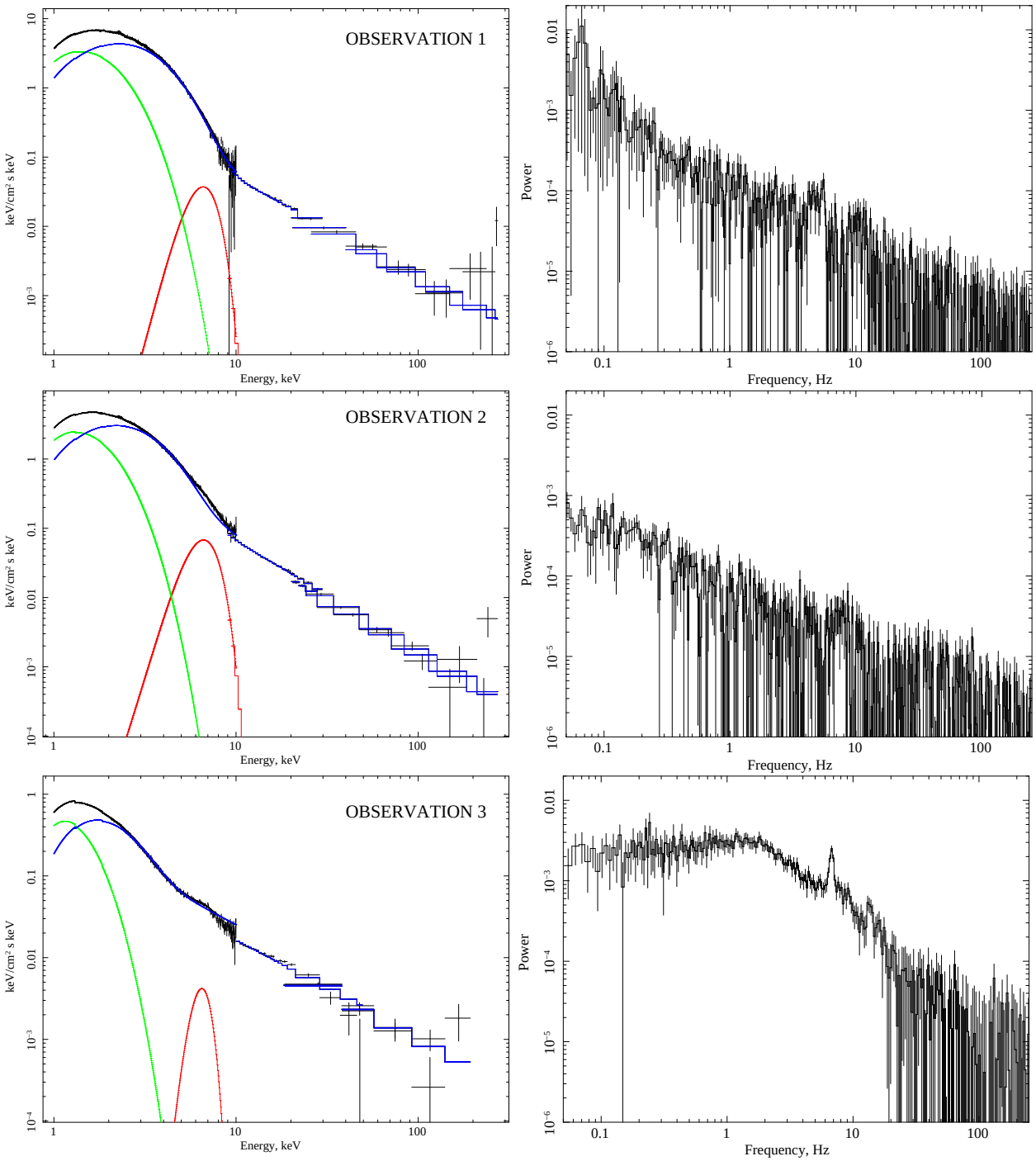

Fig. 5.— X-ray spectra (left panels) and PDS (right panels) for the XMM-*Newton*/*RXTE* observations. Note that PDSs shows the variability features (white-red noise, QPO and break frequencies) when the line is weak (see bottom panels). On the other hand PDSs are featureless when the line is strong (see top and middle panels).

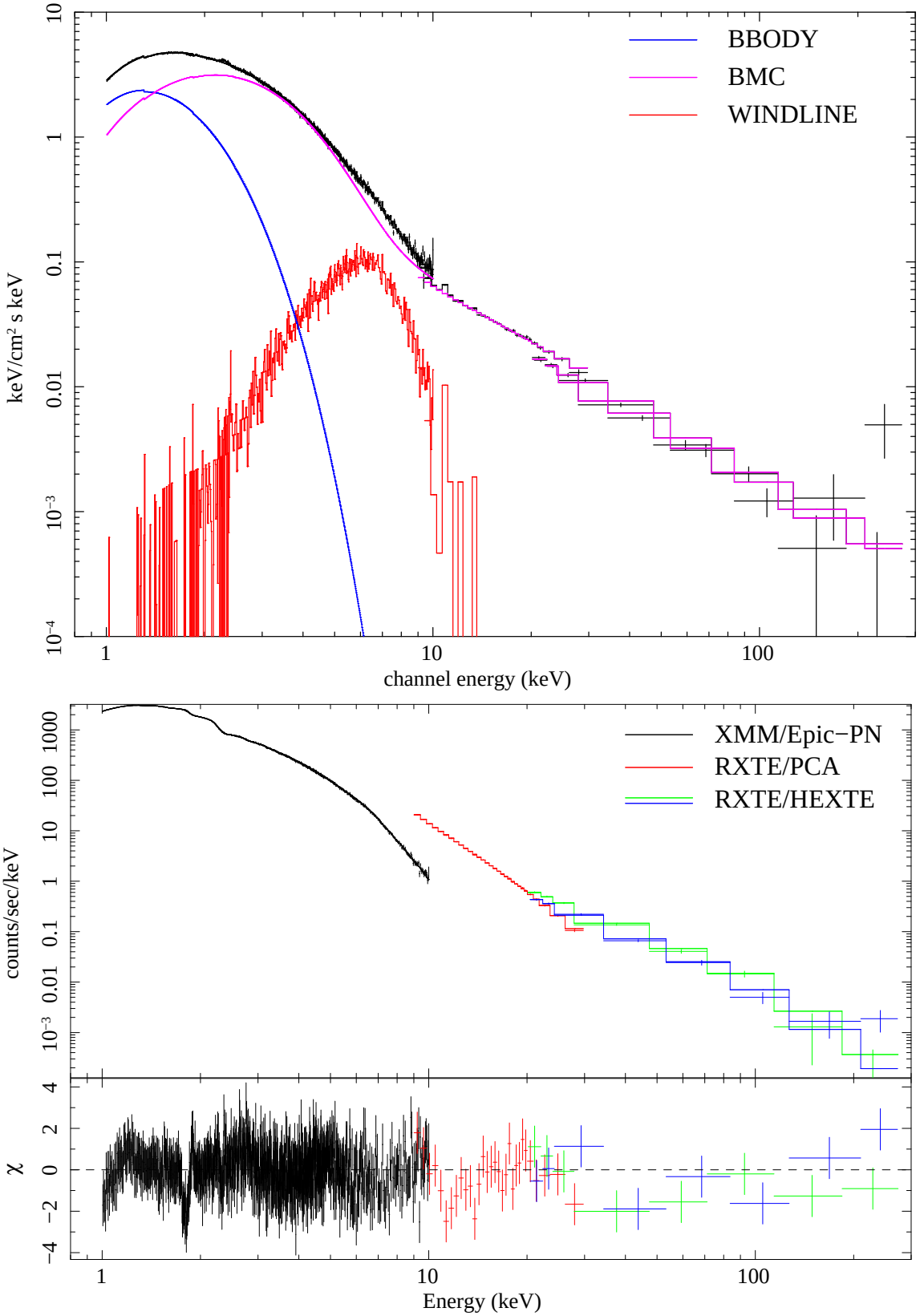

Fig. 6.— The XMM-*Newton* and *RXTE* joint observation of GX 339-4 on September 29, 2002 (Observation 2). Here we have used the best-fit XSPEC model wabs∗(BMC+BB+GAUSSIAN+WINDLINE) (see Table 4). In the top panel we show unfolded spectrum where different colors indicate different model components. The bottom

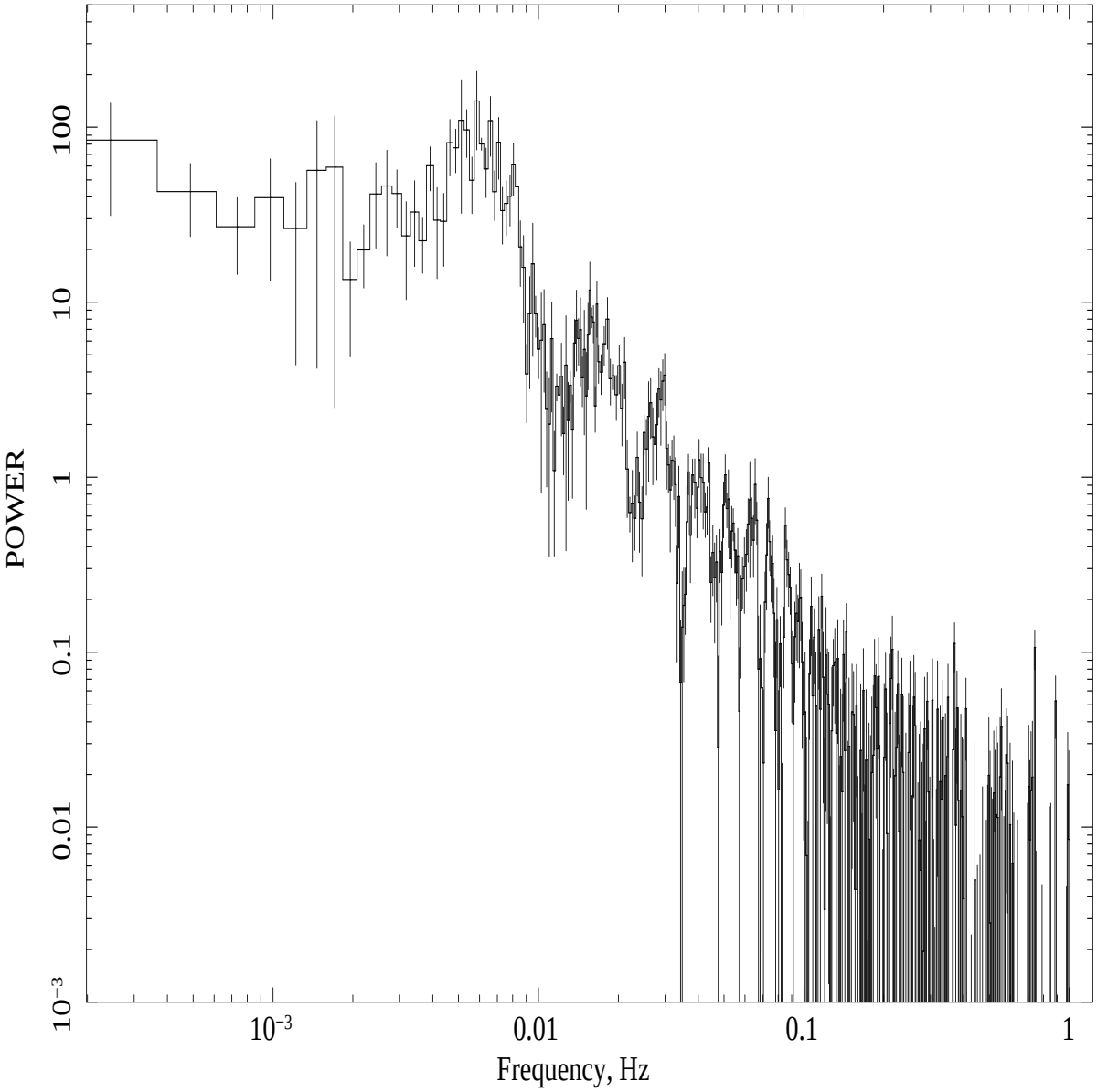

Fig. 7.— XMM PDS related to GK Per photon spectrum (see Fig. 2). One clearly see that there is no variability for frequencies higher than 0.03 Hz.

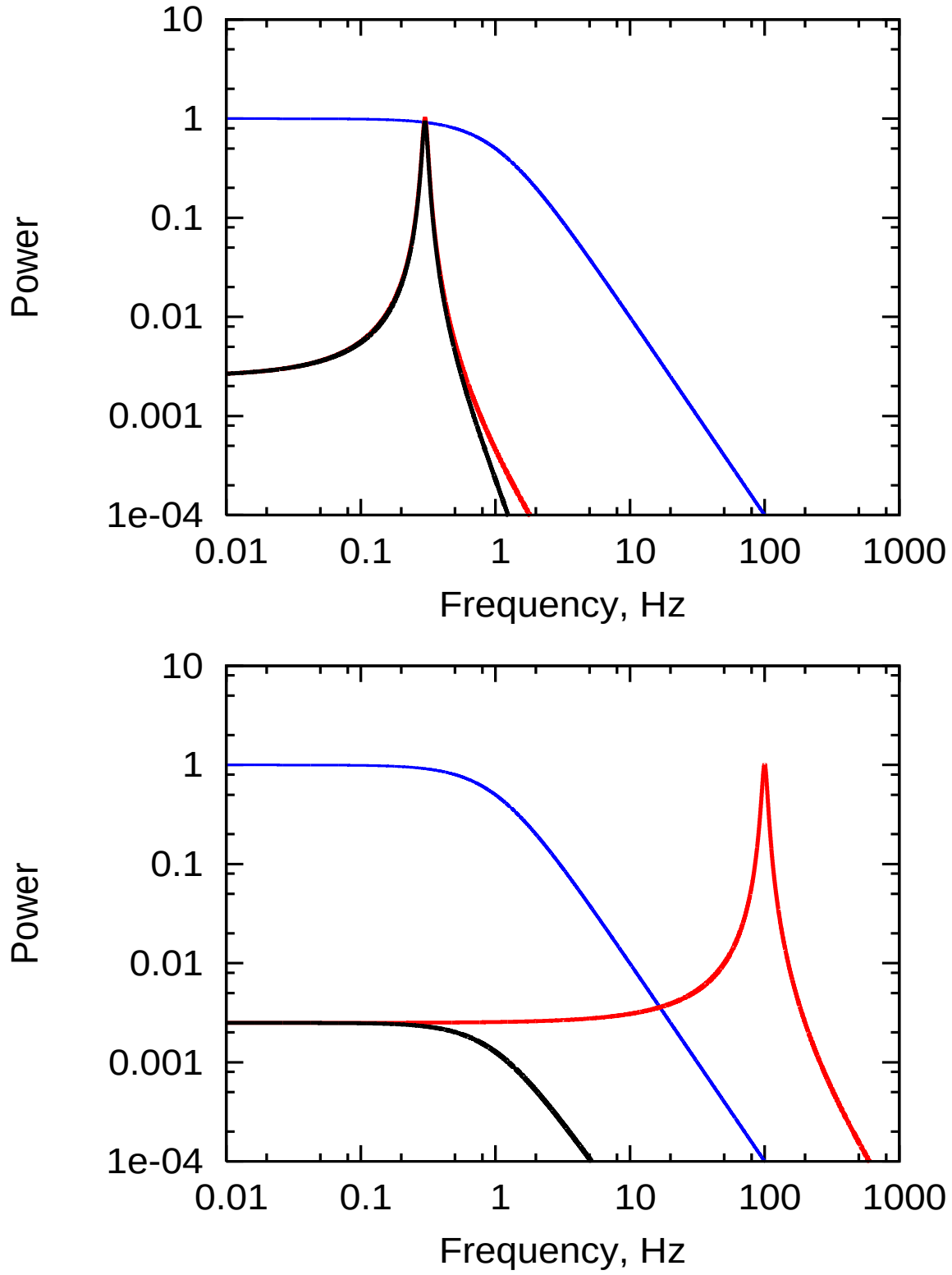

Fig. 8.— Photon scattering effect in the wind cloud. Blue line stands for the PDS related to the wind response (exponential shot) due to photon scattering. Red line describes the QPO PDS profile. Black line is the resulting PDS as a product of the wind PDS and the QPO Lorentzian. *Upper panel*: Low frequency is unaffected by the photon scattering in wind. *Lower panel*: the QPO features are completely washed in the wind if a characteristic QPO

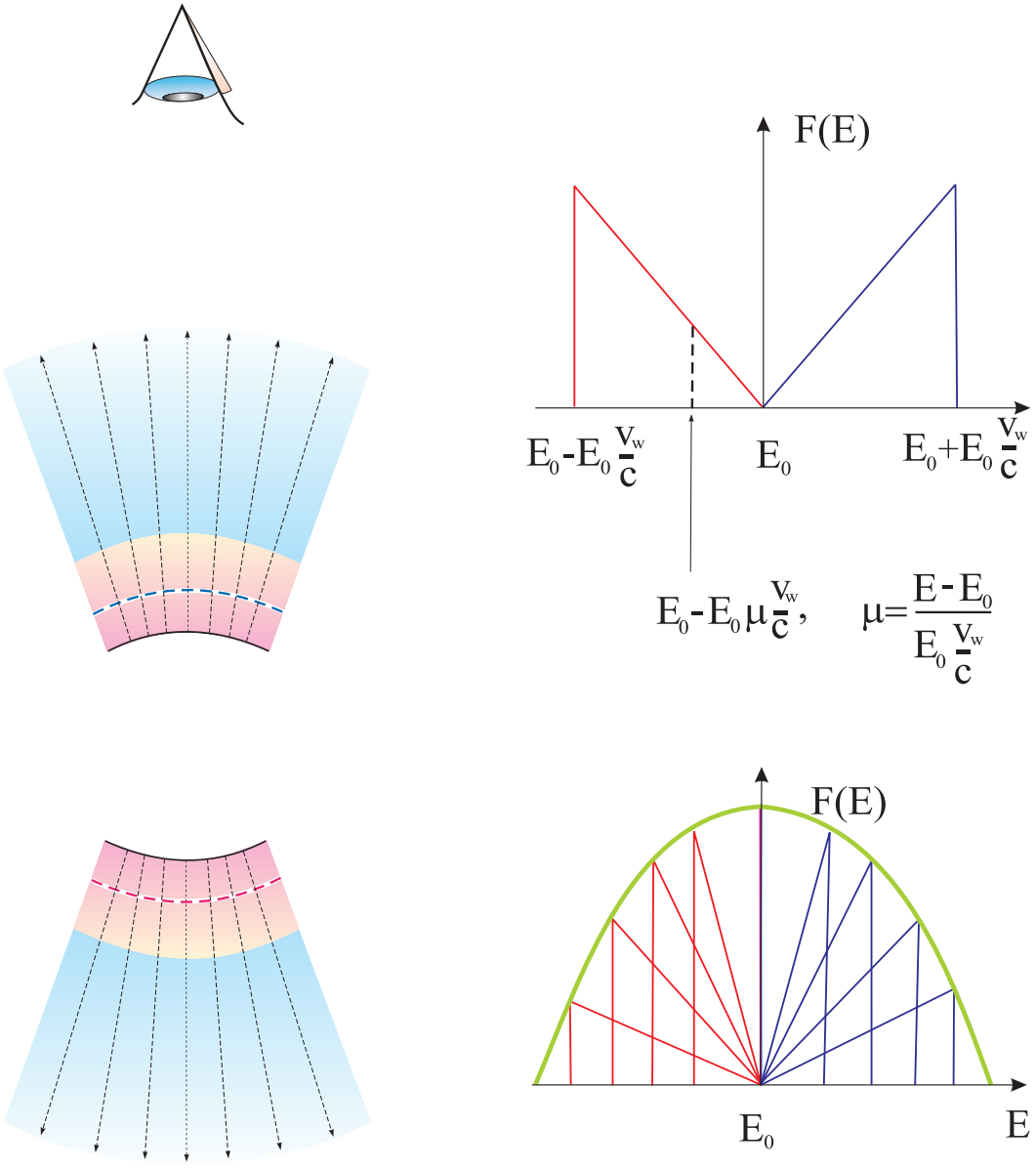

Fig. 9.— Spherical wind geometry and wind line profiles of direct component.